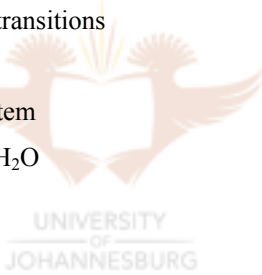


# TABLE OF CONTENTS

<b>TABLE OF CONTENTS</b> .....	<b>i</b>
<b>LIST OF FIGURES</b> .....	<b>iv</b>
<b>LIST OF TABLES</b> .....	<b>x</b>
<b>ACKNOWLEDGEMENTS</b> .....	<b>xi</b>
<b>ABSTRACT</b> .....	<b>xii</b>
<b>CHAPTER 1</b> .....	<b>1</b>
<b>INTRODUCTION</b> .....	<b>1</b>
1.1 Locality	1
1.2 Mining History	2
1.3 Background and Objectives	2
1.4 Previous Studies	4
<b>CHAPTER 2</b> .....	<b>7</b>
<b>GEOLOGICAL SETTING</b> .....	<b>7</b>
2.1 Amazonian Craton	7
2.2 Mineralization	10
2.3 Geology of the Amapa Province	12
2.4 Geology of the Serra do Navio Deposit	12
2.4.1 Stratigraphy	12
2.4.1.1 The Basement	15
2.4.1.2 The Jornal Formation	15
2.4.1.3 The Serra do Navio formation	15
2.4.2 Structure	18
2.4.3 Drill Core logs	19
<b>CHAPTER 3</b> .....	<b>21</b>
<b>PETROGRAPHY AND MINERALOGY</b> .....	<b>21</b>
3.1 Biotite schist	22
3.1.1 Mesoscopic Description	22
3.1.1 Microscopic Description	22
3.2 Graphite Schist	26
3.2.1 Mesoscopic Description	26
3.2.2 Microscopic Description	26
3.3 Mn-carbonate schist	30
3.3.1 Mesoscopic Description	30
3.3.2 Microscopic Description	30
3.4 Mn-calcite Marble	35
3.4.1 Mesoscopic Description	35



3.4.2 Microscopic Description	35
3.5 Rhodochrosite Marble	39
3.5.1 Mesoscopic Description	39
3.5.2 Microscopic Description	40
3.6 Mineral Paragenesis and Discussion	43
<b>CHAPTER 4 .....</b>	<b>47</b>
<b>FLUID INCLUSION STUDIES .....</b>	<b>47</b>
4.1 Introduction	47
4.1.1 Background	47
4.1.2 Basic Principles	47
4.1.3 Common Fluids in metamorphic rocks	50
4.1.4 Importance of Fluid Inclusions and their application in the study of metamorphic rocks	51
4.2 Analytical techniques	51
4.2.1 Sample selection	51
4.2.2 Microthermometry	52
4.3 Results	53
4.3.1 Fluid Inclusion types and phase transitions	53
4.3.2 Type 1 inclusions: H <sub>2</sub> O – NaCl	55
4.3.3 Type 2 inclusions: Pure CH <sub>4</sub> system	56
4.3.4 Type 3 inclusion: Mixed CH <sub>4</sub> – H <sub>2</sub> O	56
4.4 Interpretations and discussion	59
4.4.1 Chronology	59
4.4.2 Fluid Separation	62
4.4.3 P – T conditions of entrapment	63
4.4.4 C – O – H Calculations	66
4.4.4.1 Introduction	66
4.4.4.2 Methods	67
4.4.4.3 Results	68
<b>CHAPTER 5 .....</b>	<b>71</b>
<b>GEOCHEMISTRY .....</b>	<b>71</b>
5.1 Results	71
5.1.1 Major Element Geochemistry	71
5.1.1.1 Alumo – Silicate rocks	72
5.1.1.2 Carbonate rocks	72
5.1.2 Trace element geochemistry	78
5.1.2.1. Alumo-silicate rocks	78
5.1.2.2 Carbonate rocks	80



5.1.3 Rare Earth Element Geochemistry	84
5.1.3.1 Alumo-silicate rocks	85
5.3.1.2 Carbonate rocks	88
5.2 Discussion	89
5.2.1 Alumo-silicate rocks	89
5.2.2 Carbonate rocks	90
5.3 Summary	94
5.4 Stable Isotope Geochemistry	97
5.4.1 Results	98
5.4.2 Discussion	98
<b>CHAPTER 6 .....</b>	<b>102</b>
<b>DISCUSSION AND CONCLUSIONS.....</b>	<b>102</b>
6.1 Possible protolith succession	102
6.2 Depositional model	105
6.3 Metamorphism	110
6.4 Conclusions	111
<b>REFERENCES .....</b>	<b>112</b>
<b>APPENDIX ONE.....</b>	<b>119</b>
A.1. 1 X-ray Powder diffraction analyses	119
A.1.2 Optical microscopy	120
A.1.3 Scanning Electron Microscopy (SEM)	120
A.1.4 Fluid inclusion studies	120
A.1.5 Whole rock geochemistry	121



# LIST OF FIGURES

- Fig.1.1: Location map of the Serra do Navio deposit, Amapá Province, Brazil. 1
- Fig.1.2: Location of open cast sections at the Serra do Navio deposit. Modified from Rodrigues et al. (1986). 3
- Fig.2.1: The cratonic domains of Brazil, South America. All the cratons shown are part of the Amazonian Craton (After Zhao et al., 2002). 8
- Fig. 2.2: The tectonic map of Brazil; younger Phanerozoic cover masks the cratonic domains (CPRM, 2001). 9
- Fig.2. 3: Regional geology of the northern Guiana shield, showing the geologic setting of the Serra do Navio deposit. Insert shows the areal extent of the Guiana shield as well as the southern Guaporé shield. Modified after Voicu et al. (2001). 11
- Fig. 2.4: Geological map of the Amapa Province, showing all the geologic terranes that are exposed in the area. 13
- Fig. 2.5: Geologic map of the Serra do Navio deposit. Note the location of the 3 drill holes described in this study (modified after Scarpelli, 1973 and Rodrigues et al., 1986). 14
- Fig. 2.6: Cross-section along line A-B (see Fig. 2.6) at the Serra do Navio deposit. 16
- Fig.2.7: Idealized sketch map of the outcrop of the carbonate protore and the mineralized oxidized ore in the open pit. 17
- Fig 2.8: Profile across the Serra do Navio showing the inferred structure in the area occupied by drill core DH116. 18
- Fig.2.9: Drill core logs from the F-12 open pit in the northwestern section of the Serra do Navio deposit. 20
- Fig. 3.1: Hand specimen photographs of the biotite schist. A: Typical appearance with well developed bedding-parallel foliation. Microscopic studies reveal that quartz and plagioclase alternate with biotite to define the lamination (DH114-N). B: Medium-grained pale gray biotite schist very rich in plagioclase (DH116-P). C: Gentle open centimetric micro folds in plagioclase and quartz rich (light colored laminae) biotite schist (DH116-O). Note almost gneissic appearance of this sample. 23

Fig. 3.2: Photomicrographs (A – E) and SEM-BSE images (F) illustrating the textural relationships in biotite schist. A: Growth zoning in spessartine poikiloblasts with inclusions in the inner core but missing from outer rim (DH114-O); B: Quartz and plagioclase filling interstitial spaces and fractures between spessartine porphyroblasts (DH140-Q); C: Discrete bands of quartz/plagioclase alternating with biotite/chlorite layers to define the foliation (DH116-R); D: Biotite laths, often restricted to the well foliated parts of the rock (D114-N); E: Very large spessartine porphyroblast cogenetic with biotite (DH116-T); F: Chalcopyrite occurring as inclusions in, and as adjacent grains around spessartine (DH140-O). 25

Fig.3.3: Hand specimens of the compact and dark colored graphite schist. A: Very fine-grained graphite schist with sulphide stringers along the foliation/bedding planes (DH114-K); B: Flaky graphite randomly oriented with biotite, quartz and sulphides (DH116-P). 28

Fig. 3.4. Photomicrographs illustrating important petrographic characteristics of graphite schist (A, D, E – photomicrographs; B, C, F – SEM-BSE images). A: Biotite and graphite flakes aligned along the foliation. (DH114-E); B: Spessartine porphyroblast intergrown with pyrite showing concomitant growth. Note the apparent rotation in the spessartine defined by pyrite (DH114-J); C: Tephroite and spessartine replaced by cobaltite (DH114-J); D: Chalcopyrite and chalcocite enclose quartz (DH114-J); E: Pyrite restricted to the foliation plane showing that it formed contemporaneous with deformation. (DH116-P); F: Pyrophanite replacing ilmenite (DH114-J). In each case the tiny black mineral flakes are graphite. 29

Fig. 3.5: Hand specimen photographs depicting several types of Mn-carbonate schist. A: Granular Mn-carbonate schist characterized by pinkish rhodonite and tephroite (DH140-A); B: Very coarse grained (~2 –5mm) sample showing intergrown rhodochrosite, rhodonite and tephroite (DH140-E); C: Coarse grained (>2mm) sample with a ~8mm rhodochrosite filled veinlet crosscutting it (DH140-C). 32

Fig. 3.6: Photomicrographs illustrating different petrographic features of Mn-carbonate schist. A: Poikiloblastic spessartine with regular edges set in a Mn-calcite matrix (DH114-A); B: Mn-calcite replacing spessartine. Note the irregular remnants of spessartine porphyroblasts (DH116-D); C: Granular rhodochrosite, subordinate to Mn-calcite associated with tephroite and rhodonite (DH116-A); D: Rhodonite and Mn-calcite replacing tephroite and regularly shaped porphyroblasts of spessartine (DH116-B); E: Coarse (>4mm) anhedral tephroite typically fractured replaced by Mn-calcite along the grain boundaries and fractures (DH140-A); F: Mn-calcite replacing tephroite (DH140-D). 33

Fig. 3.6 (contd.). G: Mutual crosscutting relationships between rhodonite and tephroite. Note the irregular remnants of Mn-calcite within the euhedral spessartine (DH114-A); H: Metamorphic assemblage of

biotite, tephroite, rhodonite, Mn-calcite and sulphides (DH116-G); I: Late pyrite constrained to the boundaries of spessartine (DH116-B); J: Medium grained granular pyrophanite with pyrite inclusions. Note the fine-grained blebs of yellow-brown alabandite on the edges of pyrophanite (DH116-G). 34

Fig. 3.7: Selected samples of Mn-calcite marble. A: Dark gray medium grained (<1mm) sample with a massive texture (DH116-A); B: Coarse-grained medium gray sample with prominent rhodochrosite vein (DH114-C); C: A mm-thick veinlet of rhodochrosite crosscuts Mn-calcite (DH116-J). 37

Fig. 3.8: Photomicrographs and SEM-BSE images depicting textural and mineralogical relationships in Mn-calcite marble. A: Quartz in sub mm-thick veinlets that crosscut a Mn-calcite rich assemblage (DH114-C); B: Tephroite porphyroblasts (~2mm) engulf and replace Mn-calcite (DH114-D); C: Mn-calcite replaces spessartine porphyroblasts. Note that the porphyroblast has older Mn-calcite inclusions and has been almost completely consumed by a younger generation of Mn-calcite (DH114-C); D: Subhedral spessartine crosscut by quartz and hosting poikilotopic inclusions of quartz, Mn-calcite and graphite (DH116-A); E: Coarse tephroite intergrown with granular Mn-calcite. (DH116-J); F: Mn-calcite replacing tephroite along the grain boundaries (DH116-J). 38

Fig. 3.9: Hand specimen photographs of selected rhodochrosite marble samples. A: Massively textured grey rhodochrosite marble with randomly oriented veinlets of rhodochrosite and quartz. Quartz is usually thicker (~3mm) and younger as it usually crosscuts rhodochrosite veinlets (DH116-M); B: Massive and granular-textured rhodochrosite marble dominated by rhodochrosite, Mn-calcite and quartz (DH114-B). 40

Fig. 3.10: Photomicrographs depicting textural and mineralogical relationships in rhodochrosite marble (A – C, thin sections; D – F SEM-BSE). A: Granoblastic rhodochrosite with minor spessartine (DH114-L); B: Poikilotopic spessartine with irregular jagged boundaries encloses carbonate and quartz (DH140-L); C: Pyrophanite and sulphide minerals “pushed” away by the growth of spessartine (DH116-I); D: Chlorite replacing spessartine showing evidence of retrograde reactions (DH140-L); E: Large euhedral crystal of cobaltite with inclusions of tephroite (DH114-B); F: Submillimetre veinlets of chlorite and Mn-calcite crosscutting an aggregate of tephroite, which has rhodochrosite inclusions (DH140-N). 42

Fig. 3.11: Mineral paragenesis chart for the Serra do Navio deposit. Abbreviations: (Rhd-i, ii, iii): 1<sup>st</sup>, 2<sup>nd</sup> and 3<sup>rd</sup> generation rhodochrosite respectively, (Mnc-i, ii, iii): 1<sup>st</sup>, 2<sup>nd</sup> 3<sup>rd</sup> generation Mn-calcite respectively, (Qtz-i, ii, iii): 1<sup>st</sup>, 2<sup>nd</sup> and 3<sup>rd</sup> generation quartz; (S-i, ii, iii): 1<sup>st</sup>, 2<sup>nd</sup> and 3<sup>rd</sup> generation

sulphide respectively. \* Includes both sedimentation and diagenesis. NB: Only the relevant mineral phases are included in the chart. 45

Fig. 4.1: The P – T evolution of an aqueous fluid inclusion trapped at some pressure and temperature, then subsequently cooled down along a path of constant density (or molar volume, i.e. an isochore. S = Solid, L = Liquid, V = Vapor, Th = homogenization temperature, Pt – Tt = Pressure and temperature at the Triple point of water; cp = critical point. 48

Fig. 4.2: Phase diagram for the system H<sub>2</sub>O – NaCl. An aqueous fluid inclusion with a salinity of ~ 8 wt. % NaCl is heated from freezing. This inclusion reaches the invariant eutectic point at –21.1 °C when all the hydrohalite is consumed. Then it follows the liquidus until the final melting of the ice at about –5 °C. Note that the salinity determines which fields are entered into at certain phase transitions (modified after Greyling et. al, 2001). 55

#### \_Toc95620015

Fig: 4.3b: Typical fluid inclusions identified in spessartine at the Serra do Navio deposit. A and B: Type 1 low-salinity inclusions of the H<sub>2</sub>O – NaCl system. C and D: Type 2 inclusion of the pure CH<sub>4</sub> system; E and F: Type 3 mixed inclusions of the CH<sub>4</sub> - H<sub>2</sub>O system. 58

Fig. 4.4: Microthermometric results for Type 1 inclusions represented by histograms. A: Temperatures of phase transitions with initial temperatures of melting ( $T_{mi}^{ICE}$ ); B: Temperatures of phase transitions with final temperatures of melting ( $T_{mf}^{AQ}$ ); C: Temperatures of phase transitions with temperatures of homogenization to the liquid phase ( $T^h^{AQ}$ ). In each case the total number of fluid inclusions is 59. 60

Fig. 4.5: Binary plot of the final melting temperatures plotted against homogenization temperatures of Type 1 inclusions (n = 59). 61

Fig. 4.6: Microthermometric results for Type 2 (CH<sub>4</sub>) inclusions. Histogram depicts the homogenization temperature of methane to the liquid phase. 61

Fig. 4.7: Microthermometric results for Type 3 (CH<sub>4</sub> – H<sub>2</sub>O) inclusions. Histogram depicts the homogenization temperature of the mixed carbonic – aqueous inclusions to the liquid phase. These inclusion types are least in abundance. 62

Fig. 4.8: Isochores for Type 1 and Type 2 inclusions. In each case the end members of homogenization temperatures are taken. The shaded light gray area indicates the intersection of this range and theoretically represents the possible P – T region of entrapment of the fluid inclusions. 64

- Fig. 4.9: Fluid distribution in the continental crust as inferred from fluid inclusion studies (after Touret and Dietvorst (1983) 66
- Fig: 4.10: Isobaric-isothermal diagram illustrating the variation of mole fraction of water (solid line) and oxygen fugacity (dashed line) with changing for a carbon saturated C-O-H fluid. For a fluid of  $XCO_2/(XCO_2 + XCH_4) = 0.1$  the typical  $XH_2O$  and  $fO_2$  are shown. 70
- Fig: 4.11: Isobaric-isothermal diagram illustrating the variation of mole fraction of water (solid line) and oxygen fugacity (dashed line) with changing for a carbon saturated C-O-H fluid. For a fluid of  $XCO_2/(XCO_2 + XCH_4) = 0.1$  the typical  $XH_2O$  and  $fO_2$  are shown. 70
- Fig.5.1: Binary plots (wt.%) illustrating the major element geochemistry of the alumo-silicate group of rocks from the Serra do Navio deposit. Note the complete overlap of major element geochemistry of both lithologies and negative correlation of  $SiO_2$  with all other major elements with the exception of MgO and CaO. 75
- Fig.5.2: Binary plots (wt.%) illustrating the major element geochemistry of the Mn-carbonate-rich group of rocks from the Serra do Navio deposit. The three petrologically distinct lithologies consistently plot in particular fields. With the exception of MnO, all major elements have a positive correlation with  $SiO_2$ . 76
- Fig.5.3: Ternary plots (wt. %) contrasting the major element geochemistry of the alumo-silicate and carbonate-rich groups of lithologies. A: Mn-Si-Ca: The three petrologically distinct carbonate rich lithologies plot in well-defined non-overlapping fields. The biotite schist and graphite schist data in contrast occupy the same field, but are well removed from the carbonate-rich lithologies. B: Mn-Si-Al: The difference between the carbonate-rich lithologies is clearly due to negative covariation between Mn and Si. Note Mn-poor but Al-enriched composition of biotite schist and graphite schist. C: Mn (Ca + Mg) – Fe. The three corners represent carbonate constituents. The three carbonate-rich lithologies overlap whereas the alumo-silicate rocks scatter widely. 77
- Fig. 5.4: Spider diagram of Upper Continental Crust (UCC) - normalized trace element concentrations of different lithological groups of the Serra do Navio deposit. UCC = 1. A: Biotite schist. Most elements plot close to upper continental crustal estimates; B: Graphite schist. Very similar to biotite schist with most trace elements ~1 except for a marked enrichment in Ba; C: Rhodochrosite marble; D: Mn-calcite marble; E: Mn-carbonate schist. All carbonate rich rocks are depleted in most trace element concentrations with respect to UCC (Taylor and McLennan, 1981). 80



- Fig.5.5: Binary plots of trace elements of the different lithological groups of the Serra do Navio deposit. A:  $K_2O$  vs. Rb; B: K vs. Ba; C: MnO vs. Ba; D:  $Al_2O_3$  vs.  $\Sigma REE$ ; E: V vs. MnO; F: Co vs. MnO; G: MnO vs.  $Ce^*$ ; H:  $TiO_2$  vs. Zr. 81
- Fig.5.6: PAAS normalized REE patterns for whole rock analyses of the different lithological groups of the Serra do Navio deposit. A: Biotite schist; B: Graphite schist; C: Rhodochrosite marble; D: Mn-calcite marble; E: Mn-carbonate schist. 88
- Fig. 5.7: A ternary diagram of  $(Ni + Co + Cu)*10 - Mn - Fe$  for the Mn-rich carbonate rocks of the Serra do Navio deposit. These carbonate rocks occupy the Mn-rich corner of the hydrothermal field. Also shown are the fields for modern hydrogenetic and hydrothermal Fe – Mn crusts and nodules (Diagram after Bonatti et al., 1972). 93
- Fig.5.8: The binary MnO –  $SiO_2$  plot reveals the presence of the four distinct geochemical groups in the sample set from the Serra do Navio deposit. (a): Rhodochrosite marble; (b): Mn-calcite marble; (c): Mn-carbonate schist; (d): Alumo-silicate rock. 94
- Fig. 5.9: Diagram used to determine hydrothermal vs. detrital component based on Al/Ti and Fe-Mn content. Modified after Peter and Goodfellow (1996). 95
- Fig. 5.10: Diagnostic plots to differentiate sedimentary manganese deposits from different depositional environments (after Nicholson, 1992). “Dubhite” = supergene Mn-oxyhydroxide accumulations formed at the expense of base metal mineralization (Nicholson, 1992). Rooinekke Formation data from Gutzmer and Beukes (1998a) and Hotazel Formation data from Van Staden (2002). 96
- Fig. 5.11: Stable isotope composition ( $\delta^{18}O$  vs.  $\delta^{13}C$ ) of the Mn-carbonates at Serra do Navio deposit. 100
- Fig. 5.12: Plot of  $\delta^{18}O$  vs.  $\delta^{13}C$  for the carbonate rocks at Serra do Navio in comparison to other manganese carbonate deposits. 100
- Fig.6.1: Profile across the three drill cores at the Serra do Navio deposit 103
- Fig. 6.2: Idealized depositional model of the host rock succession at Serra do Navio. Pelitic sediments are deposited first, followed by chert and Mn, then Mn only. Carbonaceous sediments accumulate in deeper water environments, under dys- to anaerobic conditions. Model based on Frakes and Bolton (1992). 107

Fig.6.3: Idealized model for the deposition and facies relationships of the rocks at the Serra do Navio deposit. Model modified after Leube et al. (1990). 108

Fig.6.4 Idealized section from the Serra do Navio deposit correlated with a true stratigraphic section from the Nsuta deposit, Ghana with an interpretation of predicted sedimentary sequences that constitute the deposits. 109

## LIST OF TABLES

Table 1.1: Stratigraphic column of the Serra do Navio deposit (Scarpelli, 1973)	5
Table 2.1: The revised nomenclature of the lithologies at Serra do Navio.	17
Table 3.1: Mineralogy of biotite schist from petrographic studies and X-ray powder diffraction.	24
Table 3.2: Mineralogy of graphite schist as determined by petrography and X-ray powder diffraction.	27
Table 3.3: Mineralogy of Mn-carbonate schist as determined by petrographic studies and X-ray powder diffraction.	31
Table 3.4: Mineralogy of Mn-calcite marble from petrographic studies and X-ray powder diffraction.	36
Table 3.5: Mineralogy of rhodochrosite marble as determined by petrography and X-ray diffraction.	39
Table 4.1: The host minerals and associated rock types selected for fluid inclusion studies.	52
Table 4.2: General characteristics of the fluid inclusion types observed in spessartine at Serra do Navio deposit.	54
Table 4.3: Input and output data for the calculation of the equilibrium composition of a carbon saturated C-O-H fluid of which at 1000 bar and 400°C.	68
Table 4.4: Input and output data for the calculation of the equilibrium composition of a carbon saturated C-O-H fluid of which at 2000 bar and 500°C.	69
Table 5.1: Major element geochemistry of alumo-silicate rocks from the Serra do Navio deposit. NB: All data in wt. %.	73
Table 5.2: Major element geochemistry of carbonate rocks from the Serra do Navio deposit. NB: All data in wt. %.	73
Table 5.3: Trace element geochemistry of alumo-silicate rocks at the Serra do Navio deposit. All data in ppm.	79
Table 5.4: Trace element geochemistry of carbonate rocks at the Serra do Navio deposit. All data in ppm.	82
Table 5.5: Rare earth element concentration of selected samples of alumo-silicate rocks from the Serra do Navio deposit. All data in ppm.	85
Table 5.6: Rare element geochemistry of selected samples of carbonate rocks from the Serra do Navio deposit. All data in ppm.	86
Table 5.7: Stable isotope geochemistry and relative abundance of the carbonates in selected whole rock samples from drill core DH114, DH116 and DH140.	99

## ACKNOWLEDGEMENTS

The National Research Foundation of South Africa and the Department of Geology at the Rand Afrikaans University are thanked for the financial support.

Thanks are also due to Prof. Jens Gutzmer for all the valuable criticisms and suggestions to the research project. Thank you to Prof. Nic Beukes for all the insights and encouragement. Thank you to Dr. Jan-Marten Huizenga who is especially thanked for his excellent contribution to the chapter on Fluid Inclusion studies.

All the members of staff and the post-graduates in the Department of Geology at the Rand Afrikaans University are gratefully acknowledged for their support, direct and indirect. Additionally the staff at *Spectrau* is acknowledged for availing the equipment for use in analysis.

Finally, I wish to thank my family for all the support, patience and encouragement.



## ABSTRACT

The Serra do Navio manganese deposit is situated in Amapá Province, Brazil to the north west of the Amazon delta. This study presents results of an investigation into the lithostratigraphy, whole rock geochemistry and petrology of the ore-bearing metasedimentary rocks. The results are used to define a possible sedimentary protolith succession.

The metasedimentary succession at the Serra do Navio deposit is constituted of biotite schists, graphitic schists, Mn-carbonate schists, rhodochrosite marbles and Mn-calcite marbles. Biotite schist is characterized by biotite, plagioclase and quartz. It displays a well-preserved compositional layering. Biotite schist is interpreted to be a metamorphosed equivalent of shale or greywacke or volcanoclastic lithologies. A similar mineralogical assemblage to biotite schist dominates graphite schist, but it contains conspicuous amounts of graphite as well as a distinct foliation. For this reason it is interpreted to be derived from carbonaceous shale. Mn-carbonate schist is a massive coarse-grained rock characterized by an abundance of Mn-carbonates and Mn-silicates, i.e. tephroite, rhodonite and spessartine. It is interpreted to be the metamorphosed equivalent of manganese chert. Mn-calcite marble is characterized by Mn-calcite and rhodochrosite with subordinate tephroite, spessartine and rhodonite an assemblage thought to originate from a manganese carbonate rock with minor clay component. Rhodochrosite marble represents the most Mn-rich end member of the carbonate lithologies. It is characterized by abundant granular textured rhodochrosite and minor or no spessartine and biotite. Its protolith was almost certainly a manganese carbonate mud rock.

Fluid inclusion studies in peak metamorphic spessartine garnet at the Serra do Navio characterize three types of fluids: Type 1: an aqueous oversaturated fluid ( $\text{H}_2\text{O} - \text{NaCl}$ ) Type 2: pure  $\text{CH}_4$  and Type 3: Mixed fluids ( $\text{H}_2\text{O} - \text{CH}_4$ ). The original fluid contained heterogeneously trapped  $\text{CH}_4$  and  $\text{H}_2\text{O}$ , and then by a process of unmixing produced a mixed fluid of  $\text{CH}_4\text{-H}_2\text{O}$ . Pressure and temperature trapping conditions are constrained at 1 – 2 kbar and 400 – 500°C. This corresponds to depths of ~ 4.2 – 5.7km at which peak metamorphism occurred.

Whole rock geochemistry shows that the carbonate lithologies and the aluminosilicates plot well removed from each other. High MnO, CaO, MgO, Co, Zn and positive Ce anomalies, characterizes the carbonate lithologies. Negative  $\delta^{13}\text{C}$  values for whole rock carbonate samples illustrate that both inorganic and organic carbon were involved in the formation of the Mn-

carbonate and point to a diagenetic origin for the carbonates. Positive Ce anomalies confirm that the Mn-carbonates formed from diagenetic transformation of Mn-oxyhydroxides. The aluminosilicate rocks on the other hand are marked by high SiO<sub>2</sub>, TiO<sub>2</sub>, Al<sub>2</sub>O<sub>3</sub>, Zr and Sc as well as high  $\Sigma$ REE reflecting high clastic input. The high  $\Sigma$ REE, weak negative Eu anomaly and fairly flat REE distribution pattern all point to an old Upper Continental Crustal (UCC) provenance for the aluminosilicate rocks.

In the succession at the Serra do Navio deposit, the clastic sediments are at the base, gradually fining upwards and are succeeded by chemical sediments marking a major transgressive depositional event, which culminated in the deposition of Mn-carbonates when siliciclastic input into the basin was at a minimum. It is proposed that the siliciclastic/volcaniclastic sediments were the first to be deposited, as turbidites. Then, due to a major transgression manganese and chert were deposited with minimum terrigenous influx. The deposition sequence was capped by deposition of carbonaceous shale that was deposited under deeper water from an anoxic water column.

The depositional model for the Serra do Navio deposit is very similar to that of the weakly metamorphosed and non-metamorphosed manganese carbonate and manganiferous chert deposits of Paleoproterozoic and Phanerozoic age.

